Hydrodynamics of Reverse Metering Flows

F. J. Wang*, P. Morehouse, J. F. Knapp*, and G. A. Domoto

Xerox Corporation, Wilson Center for Research and Technology, Webster, New York

A two-roller system, consisting of an image bearing roll and a biased metering roll, is a common design for liquid ink electrophotography. To stabilize toned images, the development system is required to minimize the liquid content of the toned images. The reverse metering roll, moving in a direction opposite to the process direction, provides a mechanical shearing that reduces the liquid film thickness of the toned image. In this report, a discussion of the hydrodynamic metering mechanism is presented based on the study of modeling results as well as experiments. Formulation of computational models, based on the Navier-Stokes equations for free surface flows, is given followed by the description of experimental apparatus and methods. The critical parameters identified through this study include process parameters as well as geometrical and material properties (roller and gap sizes, process and metering speeds, viscosity, surface tension, etc.). The impact of the fluid flow characteristics on the final toned image attributes, such as the background cleanliness and the potential image degradation due to viscous shearing, is then discussed. Such issues can be made more apparent by examining the calculated fluid flow details.

Journal of Imaging Science and Technology 42: 562–566 (1998)

Introduction

Similar to dry powder electrophotography, image stability of a toned liquid ink image is crucial for color printing. To achieve better image stability, reduction of liquid content of a toned image by hydrodynamic metering has been identified as a very effective means of image conditioning. Hydrodynamic metering, accomplished by applying high shear stress, often takes place together with electrophoretic development as exemplified in the development nip between the two rolls in Fig. 1. A liquid ink is first applied to the image-bearing roller at a location upstream of the metering nip. A liquid layer is therefore formed between the two rollers with a front meniscus where fresh ink enters the development nip on the image roller. A good portion of the incoming ink is also driven away by the reversed metering roll leaving the development nip from the front end. Imagewise electrophoretic development takes place between the two rollers, while the metering roller is biased to remove toner from background areas. The film of a toned image is determined by the motion of the two rolls. When metering is performed effectively, the film thickness becomes significantly less than the minimum gap in the development nip. Thin metered films also help in achieving toner-free background development simply because the amount of toner in the thinner background layers is substantially less than for thicker layers. There are, however, concerns of metering causing image defects when the shear stress exceeds the yield stress that a toned image can withstand and still be held intact by electrostatic or adhesive forces.

Original manuscript received December 26, 1997

* IS&T Member

Mathematical Modeling and Numerical Scheme

A typical flow field is shown schematically in Fig. 1, where the fluid flow is confined by the two moving rigid surfaces and two free surfaces, the front-end meniscus and the metered film on the image bearing roll at the exit. The general behavior of two-dimensional incompressible, metering flows under gravity field is governed by the following nondimensional Navier-Stokes equations:

$$\frac{\partial u}{\partial x}+\frac{\partial v}{\partial y}=0, \tag{1}$$

$$\frac{du}{dt}=-\frac{\partial p}{\partial x}+\frac{1}{\mathrm{Re}}\nabla^2 u, \tag{2}$$

$$\frac{dv}{dt}=-\frac{\partial p}{\partial y}+\frac{1}{\mathrm{Re}}\nabla^2 v-\frac{1}{Fd}, \tag{3}$$

where u and v are velocity components in the Cartesian coordinates, and p is the pressure.

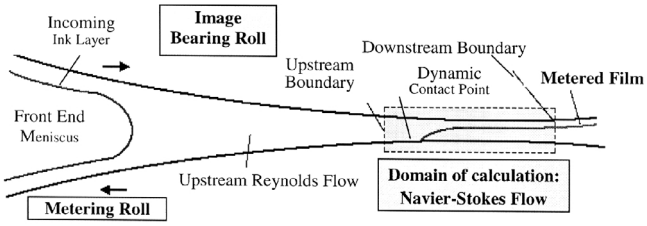

Figure 1. Schematic of a metering flow in an electrophoretic development nip.

Governing Equations. A pressure equation can be derived from the divergence of momentum (Eqs. 2 and 3), where the viscous term vanishes due to the flow incompressibility:

$$\nabla^2 p = -\left(\frac{\partial}{\partial x}\frac{du}{dt} + \frac{\partial}{\partial y}\frac{dv}{dt}\right). \tag{4}$$

The pressure of Eq. 4, together with momentum (Eqs. 2 and 3), are used as the governing equations. The Reynolds (Re) and Froude (Fd) numbers appear in the equations are

$$\mathrm{Re} = \frac{\rho U_o L_o}{\mu}, \qquad \mathrm{Fd} = \frac{U_o^2}{gL_o},$$

(where g, ρ, μ, U_o, and L_o are gravity, density, viscosity, characteristic velocity, and length.)

In this study, the process speed (speed of the image bearing roll) and the minimum gap between the two rolls are chosen to be the characteristic velocity and length.

Boundary Conditions. The boundary conditions for Eqs. 2 and 3 are (i) no slip on the rigid surface and (ii) no shear stress on the free surface. That is, using the Einstein summation notation where repeated subscripts are summed, $t_i n_j T_{ij} = 0$. Here t_i and n_i are the unit vectors in the tangential and normal directions to the free surface, and T_{ij} is the viscous stress tensor.

Regarding the boundary conditions for the pressure (Eq. 4) on the rigid surfaces, the pressure gradients, derived directly from the Navier-Stokes equations, are specified:

$$\frac{\partial p}{\partial x} = -\frac{du}{dt} - \frac{1}{\mathrm{Re}}\frac{\partial \omega}{\partial y}, \quad \frac{\partial p}{\partial y} = -\frac{dv}{dt} + \frac{1}{\mathrm{Re}}\frac{\partial \omega}{\partial x},$$

where the vorticity ω is

$$\omega = \frac{\partial v}{\partial x} - \frac{\partial u}{\partial y}.$$

The normal stress condition, as a boundary condition for Eq. 4 is applied at free surface; that is, the pressure on the free surface (neglecting the viscous stress of air due to its low viscosity),

$$p = p_{\mathrm{atm}} + \frac{1}{\mathrm{Re}} n_i n_j T_{ij} + We\left(\frac{1}{R_s}\right),$$

where the Webber number We and the radius of curvature R_s are given by

$$We = \frac{\sigma}{\rho U_o^2 L_o}, \qquad R_s = \frac{(1 + y_x^2)^{3/2}}{y_{xx}},$$

and p_{atm} and σ are the atmospheric pressure and the coefficient of surface tension.

Boundary-Fitted Coordinates and Solution Schemes. To treat the complex geometry of metering flows, a boundary-fitted coordinates method is used to generate a two-dimensional mesh for discretization of the flow equations.[1] The mesh generation is, in essence, a coordinate transformation from the irregular Cartesian plane to a regular computational plane where the two coordinates, ξ and η, are orthogonal. The mesh is numerically generated on the $\xi - \eta$ plane by a set of elliptical partial differential equations according to Thompson and co-workers.[1] The flow equations and the numerical calculation, after transforming the equations into the $\xi - \eta$ plane,[2,3] can be discretized in a rather straightforward fashion following the generic finite difference schemes. The unknown variables in the transformed equations are in their primitive form, that is, u, v, and p. A time-marching scheme is used to solve Eqs. 2 to 4. The free surfaces are moved by their present normal velocity in an explicit fashion at the end of each time step, until they reach steady state. All the other difference approximations and function values, including the governing equations and boundary conditions, are evaluated implicitly at the most recent time level. The inertial terms are treated with an Eulerian-Lagrangian method, originated by Casulli[4] and modified for boundary-fitted coordinates by Wang and Domoto.[2] All the spatial difference terms are discretized by the central difference scheme. The truncation errors are therefore first order in time and second order in space. Because the continuity Eq. 1 is not enforced explicitly, a pressure corrective scheme described by Hirt and Hallow[5] is adopted to ensure mass conservation.

Reynolds Flow Approximation and Dynamic Contact Point. Our main objective in this study is to understand the metering mechanism, that is, the hydrodynamic response of the metered film to any given variable. To achieve the goal, the numerical calculation can be performed more effectively with the following approximation. Instead of solving the full domain of the metering flow by Navier-Stokes formulation, the front-end part of the flow, as shown in Fig. 1, can be represented by a one-dimensional (1-D) Reynolds flow approximation. This is a close approximation if the front-end meniscus is distant from the dynamic contact point and the metered film. At the other end of the flow, at the downstream side, there is a dynamic contact point whose initial location is assumed and moves along the metering roll surface in time until a steady state is reached. Numerical calculations are performed in the area where a computational domain is enclosed within the rectangular box, as shown in Fig. 1. Confined by the two moving solid surfaces, the free surface of the metered film, and the upstream and downstream boundaries where the flow enters and exits the domain, the shape and location of the computational domain are treated as unknowns and obtained as part of the solution. If the downstream boundary (final metered film) is chosen to be remote from the dynamic contact point, the fluid flow at the boundary becomes simply fully developed, therefore, a fully developed flow boundary condition can be conveniently applied. The upstream boundary is treated as an interface between the two-dimensional (2-D) Navier-Stokes flow and the 1-D Reynolds flow. Iterations between the solution of Navier-Stokes and the Reynolds equations are performed and the continuity in pressure and pressure gradient is enforced until convergence is obtained.

Note that throughout this study, the contact angle has been chosen to be 100°. This assumption yields good agreement with the measured minimum film thickness. In addition, from previous experience,[6] it has been shown that the steady-state solutions can be rather insensitive to the variation of contact angle in a range. Similar observation has been made in this study, where numerical tests were done in the range of 95 to 105°.

Experimental Setup and Procedure

The experiment apparatus comprises a cylindrical image bearing roll, a reverse metering roll, a fluid application system, and a fluid removal system. The experimental

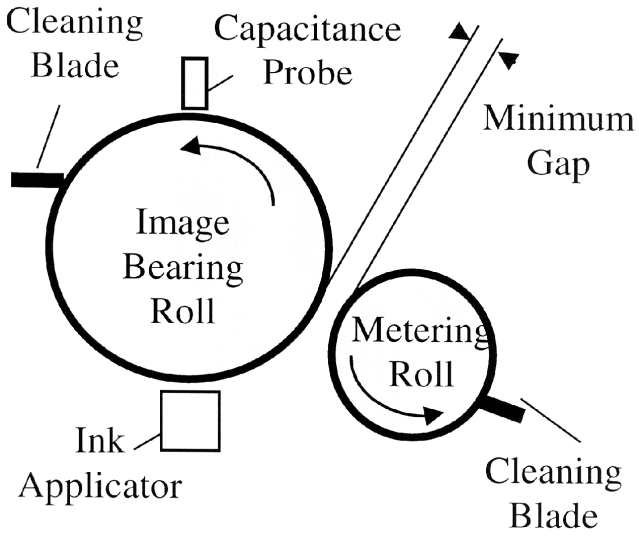

Figure 2. Schematic of experiment apparatus.

setup is shown schematically in Fig. 2. Fixture operation and data collection are computer controlled. During the experiments, a layer of fluid was deposited onto the rotating image roll and carried by the roll into a gap formed by the image bearing roll and the reverse metering roll. The thickness of the metered layer on the image roll was measured for various roll velocities, liquids, and the like. In this report, if not stated otherwise, the diameter of image roll is 9.5 in., the metering roll is 6 in., and the minimum gap is maintained at 0.003 in.

The image rolls used in these experiments were specially manufactured to minimize surface irregularities and mechanical runouts. Total runout is under 0.001 in. across the entire roll. A stepper motor provides drive to a center shaft, which supports and drives the roll. Roll velocities are computer controllable and monitored. A blade cleaner is mounted against the roll to remove the fluid from the roll surface.

The reverse metering rolls are polished steel rollers. These rolls also have total indicated runouts of less than 0.001 in. Metering gaps are maintained by wheels that contact the surface of the image roll, and the metering roll is held at a fixed distance from the image roll. The metering rolls are driven by gear motors equipped with tachometers and speed controllers. Stainless steel blades are mounted against the metering rolls to remove fluid from the roll as it rotates. The metering roll surface is clean and dry at the entrance to the metering zone.

Metered film thickness was determined in a number of ways. The simplest was to employ an "interchemical wet film thickness" gauge, a standard measurement instrument in the paint and ink industries. The gauge consists of an eccentric inner wheel supported by two outer wheels. The gauge is rolled across the wet surface until the eccentric contacts the fluid surface. The thickness is then read directly from a scale inscribed on the outer wheels. A wide variety of calibration ranges is available; for these experiments, a gauge with graduation increments of 1 μm was used.

A second technique for determination of metered film thickness takes advantage of a blade mounted against the image roll. Since the entire metered layer is removed by this blade, simply collecting and measuring the fluid results in an easy calculation of thickness.

A capacitance probe monitored continually by the controlling computer provided a third method for determining metered film thickness. This probe, a Microsense 3046 manufactured by ADE Corporation, was mounted 0.005 in. away from the image roll surface. After proper calibration to the fluid under test, this probe provided an output to the computer the thickness of the fluid layer passing the probe.

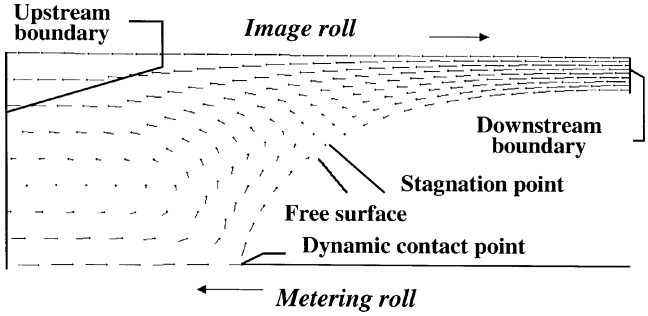

Figure 3. A vector plot of a calculated metering flow.

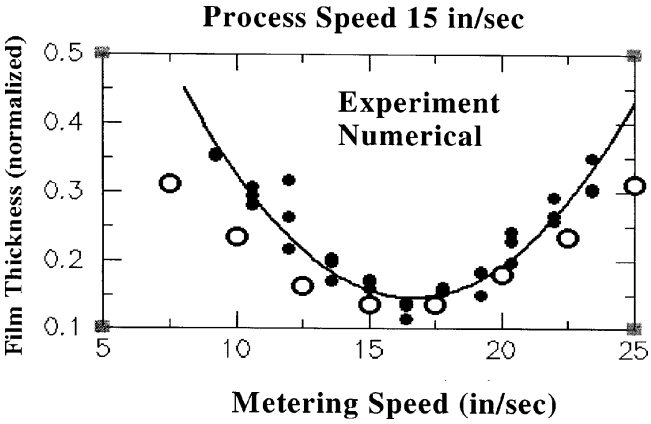

Figure 4. Metered film thickness versus metering speed.

Results

Visualization of a Metering Fluid Flow. A typical calculated metering flow field is shown in Fig. 3, a vector plot where the velocity is proportional to the length of the vector. We can see that the fluid velocity changes direction around the stagnation point on the free surface. Apparently, the fluid flow below the stagnation point is driven back to the development nip, and only a fraction of the fluid can exit to the metered film.

Major Features of the Metering Mechanism. A typical feature of the metering flow can be characterized by the plot in Fig. 4, where the metered film thickness is plotted versus the metering speed. With the present setup, including a 0.003 in. minimum gap and a 15 in./s process speed, the minimum film thickness is obtained at a metering speed around 17 in./s, a value close to the process speed. Higher or lower metering speed results in more liquid carryout. The numerical results match well with the measurement, as depicted by Fig. 4.

The metering mechanism can be better understood by examining the flow details, for example, the location of the dynamic contact point versus metering speed. Figure 5 shows five steady-state flow fields calculated with different metering speeds at a process speed of 15 in./s. The horizontal direction is the process direction. The coordinates have been normalized by the minimum gap. The

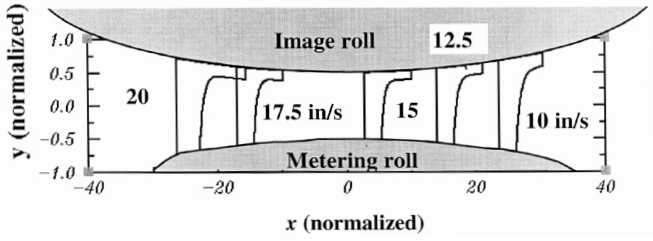

Figure 5. Locations of dynamic contact points.

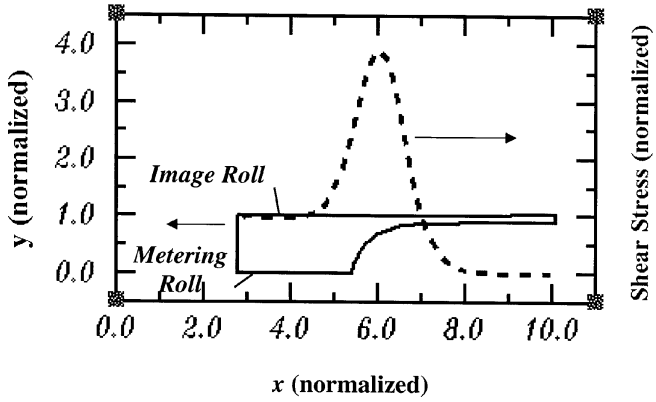

Figure 6. Shear stress distribution.

drawing is stretched in the vertical direction. Note that, as shown in Fig. 2, the flow field boundary contains a free surface, two moving solid surfaces, and one upstream and one downstream boundary. The metering speeds are 10, 12.5, 15, 17.5, and 20 in./s, associated with the flow fields displayed in Fig. 5 from right to left. The dynamic contact point changes location along the metering roll surface from right to left, passing through the minimum gap, as the metering speed is raised from 10 to 20 in./s. At 15 in./s, as the dynamic contact point settles near the minimum gap (see Figs. 3 to 5), the film thickness is reduced to the lowest of the five calculated cases.

Shear Stress on the Image Roll. The effectiveness of metering depends on the magnitude of the hydrodynamic shear stress. The shear stress distribution along the image roll is plotted in a dashed line in Fig. 6. The frame of the calculated flow field is superimposed atop the stress curve to provide a reference for location. As in the previous plot, the x and y coordinates for the fluid flow geometry are normalized by the minimum gap. The shear stress is similarly normalized, in this plot, by the shear stress at the corner of the upstream boundary and the image roll. The normalized shear stress hence has a value of one unit at the upstream corner and increases by a factor of 3 to its peak value before it decays to zero. It is interesting to note that the maximum shear occurs not at the upstream end, where it is closer to the minimum gap, but at the location around the stagnation point. This observation applies in general for flows with different metering speeds and dynamic contact locations. This observation also helps in understanding the drastic reduction in film thickness taking place near the dynamic contact point.

We then expect that by comparing the maximum shear stress for each of the five cases in Fig. 5 we ought to obtain a direct indication of the effectiveness of metering. The highest maximum shear of the five cases should give rise to the lowest liquid carryout. This belief is confirmed by the data in Fig. 7 where the stress is normalized by the maximum stress obtained in the case with a 15 in./s metering speed.

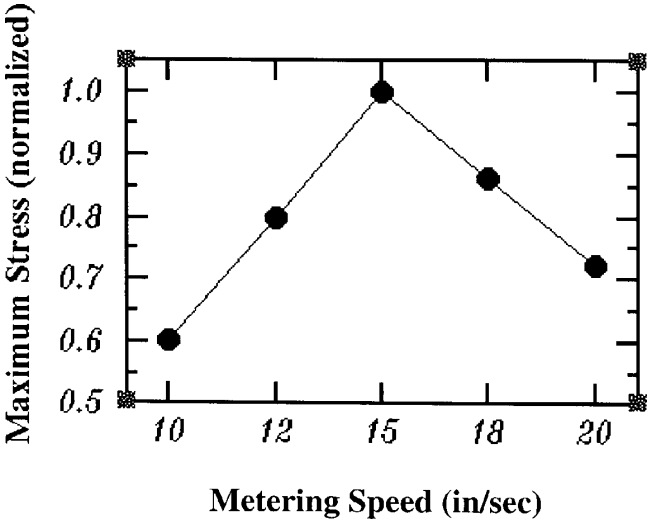

Figure 7. Maximum stress versus metering speed.

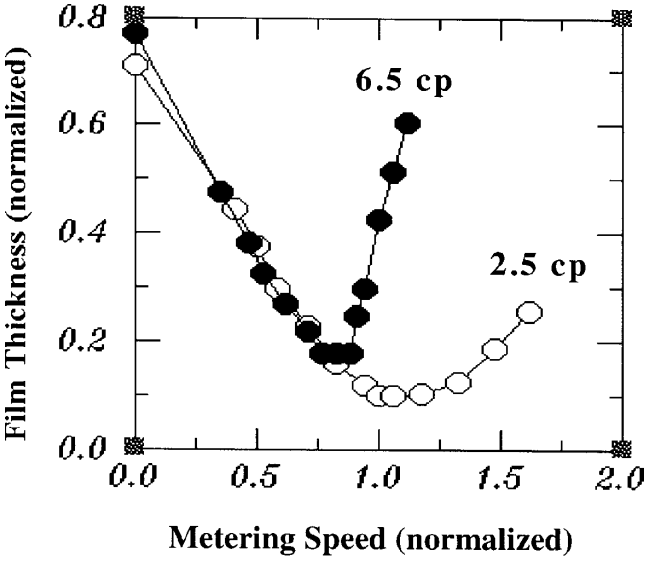

Figure 8. Experimental data of viscous effect.

Viscous Effect. One material property that has a direct influence on metering is the viscosity. In Fig. 8, experimental data were collected at process speed 17 in./s using liquids with viscosities of 2.5 and 6.5 cP. The units for vertical and horizontal axis are nondimensional after normalizing the length and velocity by the minimum gap and the process speed respectively. First, the figure shows that the minimum film thickness is higher for the more viscous liquid. Second, a salient feature is that the film thickness of the more viscous liquid is also more sensitive to the change of metering speed near the *critical speed* that minimizes the film thickness. In fact, in terms of metering performance, two liquids behave in nearly the same way when the metering speeds are below their *critical values*. The more viscous liquid, however, takes a steeper increase in film thickness when the metering speed surpasses its critical speed. Third, the critical speed is lower for the case of more viscous liquid. Similar trends have been seen from the numerical simulation, as shown in Fig. 9 where a wider viscosity range was calculated with a process speed of 20 in./s.

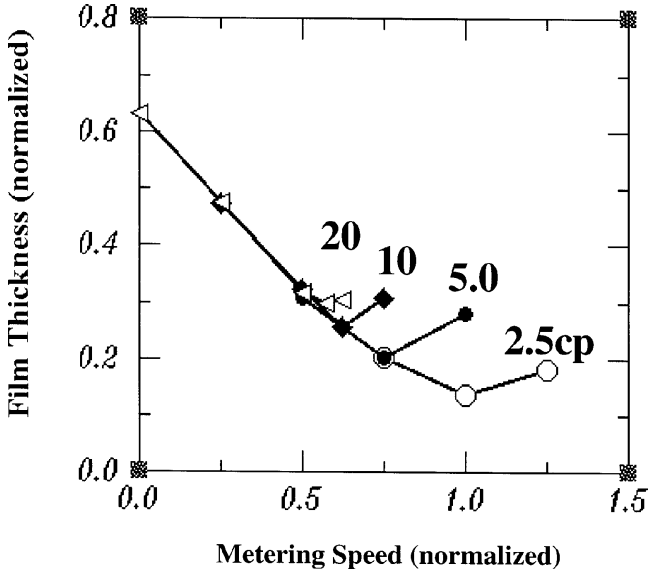

Figure 9. Computational results of viscous effect.

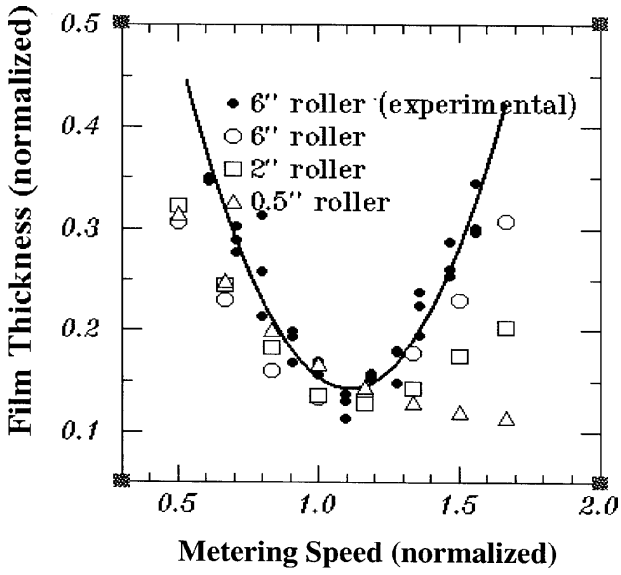

Figure 10. Effect of metering roll size.

Effect of Metering Roll Size. The size of the metering roll impacts the metering mechanism in a similar fashion as the viscous effect, as shown in Fig. 10. Changes in film thickness due to roller size start to appear only after the metering speeds exceed their critical values. Smaller rollers, similar to the less viscous liquids, tend to give a more gradual change in the film thickness as the metering speed is varied. Smaller metering rolls also require higher critical speeds as in the cases of less viscous liquids.

Background Cleaning and Image Defects. In a high-speed development system, the characteristic time for development is proportional to the length of development nip and inversely proportional to the speed. For background cleaning, however, another influencing factor is the metered film thickness. Thinner metering films help to achieve toner-free background, the area of no latent image, simply due to the fact that the distance required to move the toner away from the image-bearing member by the background cleaning field is shorter for thinner metered layers, that has been made clear by the calculated fluid flow shown Fig. 3. One constraint on metering is the possible image defect owing to higher shear. During the formation of the toned image in the development nip, the toned image is held by electrostatic force. The shear force that meters the liquid tends to shear off the toner from the image roller as well. A surge in shear stress with a magnitude of factor of 4 as the toned image exits the nip, as shown in Fig. 6, may have negative impact on image quality.

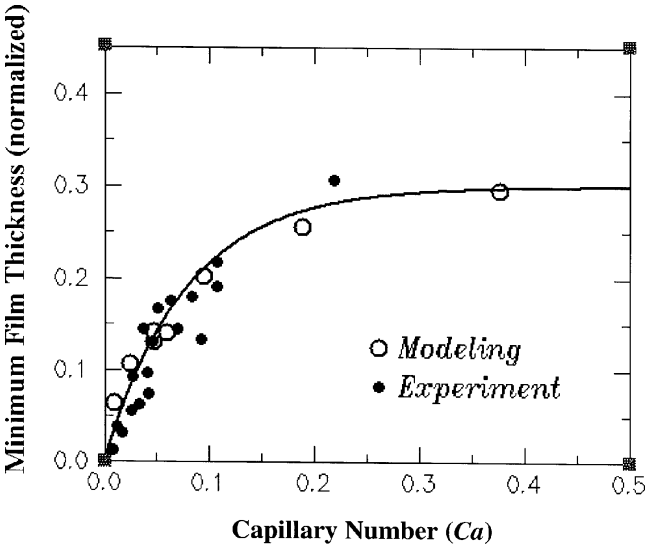

Figure 11. Film thickness = $0.3(1-e^{-12.8}\mathrm{Ca})$.

Summary

The results of the experimental and numerical study are summarized in Fig. 11, where the normalized minimum film thickness is expressed as a function of Capillary number, Ca ($=\mu U/\sigma$).

The metering mechanism has been extensively studied both experimentally and numerically. Detailed flow fields have been obtained through numerical modeling that has been experimentally verified by measuring the film thickness. With the identification of the location of the free surface and the dynamic contact point, determined by the physical geometry and process and material parameters, the mechanism of the metering flows is better understood. The verified modeling can be used as a tool for quick explorations and guide better integration of system and process design and material development. The metering model also provides a solid foundation for the next level of modeling work: electrophoretic development of liquid inks. ▲

References

1. J. F. Thompson, Z. U. A. Warsi, and C. W. Mastin, *Numerical Grid Generation*, North-Holland, New York, 1985.
2. F. J. Wang and G. A. Domoto, Free surface Taylor vortices, *J. Fluid Mech.* **261,** 169–198 (1994).
3. G. A. Domoto and F. J. Wang, Numerical simulations of charge transport in lonographic printing, *Proc. SPIE* **1912,** 197–209 (1993).
4. V. Casulli, "Eulerian-Lagrangian method for hyperbolic and convection dominated parabolic problem", *Computational Methods for Non-linear Problems,* Swansea, U.K., 1986, pp. 239–262.
5. C. W. Hirt and F. H. Harlow, A generic corrective procedure for the numerical solution of initial-value problems, *J. Comput. Phys.* **2,** 114–119 (1967).
6. F. J. Wang and G. A. Domoto, "Flow Stability Of Slot Coating—A Numerical Study", Separated and Complex Flows, FED-Vol. **217**, ASME/JSME Fluids Engineering and Laser Anemometry Conference and Exhibition, Hilton Head, South Carolina, Aug., 1995, pp. 143–150.